Bénard-Marangoni thermal oscillators: An experimental study

H. Mancini and D. Maza*

Departamento de Física y Matemática Aplicada, Facultad de Ciencias, Universidad de Navarra, 31080 Pamplona, Navarra, Spain

An experimental study of time-dependent Bénard-Marangoni convection in small aspect ratio containers and high Prandtl number fluids is presented. Two similar systems with the same aspect ratio, depth, and type of fluid are compared: one with adiabatic lateral boundaries and the other with open boundaries. In spite of the fact that very different plan forms and flows appear, both systems exhibit an oscillating plan form and a discrete narrow-band frequency spectrum in the temperature signal, having the same threshold and similar frequencies. Coincidence in temporal behavior between physical variables (temperature or velocity fields) and signals obtained from a distance representative of plan-form evolution or surface curvature is shown in the interval of the control parameter studied. The origin of a time-dependent regime arising from a boundary layer instability is discussed. Plan-form, temperature, and velocity measurements confirm this assumption, showing that this mechanism, first proposed in Rayleigh-Bénard convection, also appears under the conditions of these experiments, in time-dependent behavior of Bénard-Marangoni convection. [S1063-651X(97)04303-1]

PACS number(s): 47.20.Lz, 47.20.Bp

I. INTRODUCTION

Bénard convection [1] has been one of the most important experimental data sources in the study of spatial pattern formation [2,3]. Intrinsic interest in this kind of pattern motivates a lot of theoretical and experimental work in fluid dynamics. But since the beginning of the last decade, convection has also been considered a useful system for experimenting with new ideas in nonlinear dynamics. This kind of study was principally devoted to the examination of spatiotemporal oscillations as chaotic or preturbulent states in systems with few degrees of freedom, which enable experimenters to obtain very rich and complicated dynamic behaviors.

In thermally driven convection, movements in a fluid layer heated from below begin if a critical vertical temperature gradient overcomes dissipative forces: lateral thermal diffusion and viscosity. When the thermal gradient generates a buoyancy instability this experiment is usually called Rayleigh-Bénard convection. If the fluid layer is heated uniformly from below and cooled from above by a gas (i.e., ambient air), convection can be caused by surface tension gradients and is frequently called Marangoni convection. When buoyancy and surface tension instability both act simultaneously, the name of Bénard-Marangoni convection is normally used. Near the convection threshold, a structure of cells with a horizontal dimension comparable with depth normally appears [4,5].

A major difference exists if the lateral dimension of the system can be considered large compared with depth or not. When the horizontal extension l is comparable with the depth d, a strong influence from the lateral walls is expected. The aspect ratio, defined as $\Gamma = l/d$, is normally used to measure this influence. In small aspect ratio experiments, lateral boundary conditions determine the pattern, reducing the pos-

sibilities to a few modes compatible with the symmetries. With feebly confined geometry (large aspect ratio), the depth of the layer is the only characteristic distance in the system, and the wave number k, instead of aspect ratio, is the geometrical parameter normally used. In this case, the wave number can change continuously in the stability interval and the pattern is not heavily influenced by lateral boundaries [2].

Other important parameters are necessary to define the problem. Fluid properties, difference of temperature applied, geometry (depth of the layer and lateral boundaries dimension, symmetry, and thermal properties), and heat transfer characteristic at the upper and bottom surfaces of the fluid all change different aspects of the flow. Several nondimensional numbers have been introduced to consider their influence, the most relevant of which are as follows.

(a) The Prandtl number: $\mathrm{Pr} = \nu/\kappa$, where ν is the kinematic viscosity and κ the thermal diffusivity. It gives the ratio between thermal and velocity diffusion times. With high Prandtl number, a velocity perturbation relaxes suddenly and follows temperature variations. Temperature, density, and velocity fields then remain coupled.

(b) Rayleigh and Marangoni numbers are used to measure distance from thermal equilibrium, and their ratio gives a proportion among the causes of instability: The Rayleigh number

$$\mathrm{Ra} = \frac{\alpha g d^3}{\kappa \nu} \Delta T \qquad (1)$$

is a measure of buoyancy effects, and the Marangoni number of surface tension effects

$$\mathrm{Ma} = \frac{|\partial \sigma/\partial T| d}{\rho \kappa \nu} \Delta T, \qquad (2)$$

where ΔT is the temperature difference, g the gravitational acceleration, α the thermal expansion coefficient, κ the thermal diffusivity, $|\partial \sigma/\partial T|$ the surface tension (σ) thermal coef-

————
*Also at Departamento de Física, Universidad Nacional de San Luis, Chacabuco y Pedernera, 5700, San Luis, Argentina.

ficient, ρ the density, and d the depth of the layer. Rayleigh and Marangoni numbers have critical values corresponding to the threshold of convective movements ($Ra_c=670$ and $Ma_c=80$ in the linear theory [6], when they are considered acting independently and the Biot number $L=0$). If buoyancy and surface tension effects are both present, their effects are coupled, reinforcing each other, and giving lower threshold values [6–9], when geometry is considered not to be laterally confined.

(c) Nondimensional numbers representing other characteristics of the system, i.e., the total heat flow (Nusselt number), the heat coupling at the upper surface related to the heat conducted by the fluid (Biot number), etc. They have been sufficiently discussed in the literature [5–7], and will be defined when necessary.

In spite of whether the system is strongly confined or not, convection becomes time dependent if the temperature gradient is increased sufficiently (and then turbulent, as is well known). This state, in which one or more structures (rolls or cells) of the convective pattern oscillates, can be periodic, multiperiodic, or chaotic. The critical Rayleigh number corresponding to these secondary thresholds depends on the Prandtl number, as was shown in early publications [10]. For silicone oils with a high Prandtl number, different oscillation regimes are clearly separated, and this kind of fluid has normally been used in order to study preturbulent states in buoyancy controlled convection [11,12].

In time-dependent convection with a small aspect ratio, a discrete spectrum composed of narrow-band frequencies appears [13,14]. When the Rayleigh number is further increased from the time-dependent threshold, different transition routes to chaos have been shown, and highly reproducible results were obtained [15].

In fluids with a high Prandtl number, the existence of a discrete frequency spectrum was confirmed in [16], together with different transition routes to chaos [17]. In the experiment reported in [16], the oscillation mechanism was identified and the oscillator position localized in the convective cell by optical interferometry. These authors showed that two main frequencies appear. The first one is identified with a periodic modulation of the boundary layer thickness, a mechanism proposed previously by Howard [18]. The second frequency appears from the periodic growth of thermal plumes in the upper (cold) boundary layer. More observations concerning the first mechanism in Rayleigh-Bénard convection are reported in the literature dating from both before and after this study [19–21].

Until recently, very few experiments were performed in Bénard-Marangoni convection where a free surface is in contact with air. When the aspect ratio is large, the pattern consists of a certain number of cells (mostly hexagonal) of lateral dimension comparable with the depth of the fluid. Some defects in the hexagonal pattern normally appear when the Rayleigh number is increased beyond the convection onset.

The structure of cells that appear near threshold in Bénard-Marangoni convection with small aspect ratios (stationary patterns) have been shown in Refs. [22, 23] for different lateral symmetries. In steady state regime (under the time-dependent threshold) spatial bifurcations may exist when the Rayleigh number is increased [23]. Rotation of the structures was anticipated in Ref. [24] and preliminary experimental results have been obtained in [25] for aspect ratios near 7. With square symmetry and adiabatic boundary conditions, a set of experiments giving a very rich dynamics is presented in Refs. [26–28]. In these studies, time-dependent convection with a narrow-band frequency spectrum appears near a codimension two point [28], when a secondary threshold in the Rayleigh number is exceeded. Dynamic behavior was modeled in these experiments by using a spatial variable obtained from the plan form. This variable describes the geometrical developments in the plan form when it becomes time dependent, and was used together with symmetry arguments to construct a mathematical model. It was able to predict a chaotic behavior zone in the parameter space, not previously observed in the experiment. But a model based only on arguments of geometry and symmetry cannot give any information about oscillation frequency values and the underlying physical mechanism.

Considering that continuous power is supplied from the bottom plate and a pulsed output is obtained in the upper surface, some transient mechanism of energy storage must exist. The boundary layer is one of the few possibilities for this to come about in high Prandtl number fluids [29]. If we suppose that the mechanism responsible in time-dependent convection is similar to that reported in Rayleigh-Bénard experiments with a high Prandtl number, then frequency and time-dependent threshold must be principally related to vertical boundary conditions (that is, boundaries related to the heat coupling), and less directly to lateral geometry.

As a theoretical model derived from first principles does not yet exist, we performed several experiments in order to separate the contributions of the lateral boundary conditions (which we suppose, in our first approach, define the plan form) from the coupling of heat to the fluid (which we suppose is responsible for the temporal behavior).

These contributions can be separated if substantial changes are introduced in the experiment of Ondarçuhu *et al.* [26], which can be summed up as removing lateral walls, but keeping all the other characteristics of the system: vertical boundary conditions, aspect ratio, depth, and kind of fluid and heating power. In order to have the same aspect ratio and similar power density (W/cm^2) in the bottom plate when lateral boundary conditions are removed, it is necessary to define aspect ratio considering l to be the dimension of the *heating plate*. In this way, both systems have the same mass of fluid above the heater. The fluid in the first one appears as a closed system with adiabatic walls and will be called system A. In the second, the fluid acts as an open system that can exchange mass and heat across lateral frontiers and will be called system B (Fig. 1). Square symmetry, which extends in system A over all the fluid layer, is in system B restricted to the region near the heater. A few millimeters up (a boundary layer thickness) system B can be influenced by the container symmetry.

In the present study, the behavior of the two systems is compared. With the first system and using the same aspect ratio ($\Gamma=4.45$), we reproduce the Ondarçuhu *et al.* experiment [26], but measuring time resolved temperature instead of the variable obtained from the plan form. Developments in temperature and plan form were observed simultaneously and the dynamic behavior previously reported was recovered with this new variable. Only new results relevant to the com-
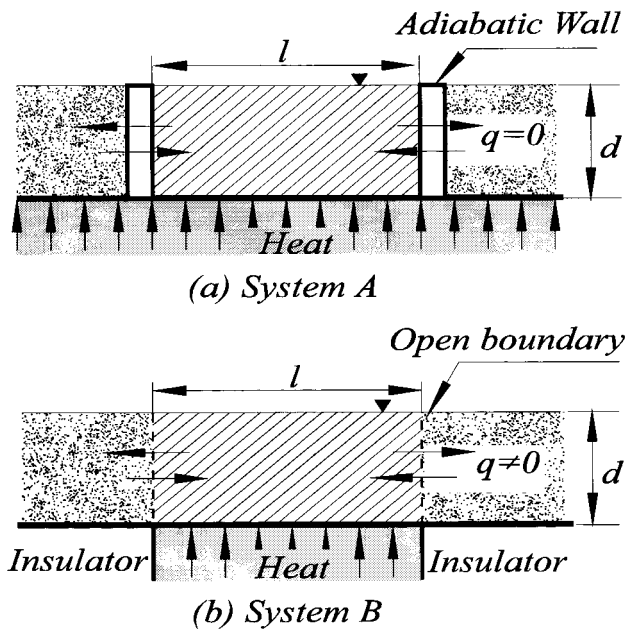
FIG. 1. (a) Cross section of system A: a fluid closed by adiabatic walls. (b) Cross section of system B; a mass of fluid with open boundaries (inhomogeneous heating).

parison are presented here. In the second system (system B) we studied previously the stationary pattern obtained for the same aspect ratio (Γ=4.45) for Rayleigh numbers from the convection onset to the time-dependent regime. When convection became time dependent in system B, signals from temperature, plan-form oscillation, and from the surface curvature were obtained and compared. As will be shown in Sec. II, the onset for the time-dependent regime is close to that in system A, and furthermore, a narrow-band frequency spectrum with similar mean period is obtained.

The experimental setup and results on stationary patterns near the second threshold in both systems is presented in Sec. II. Time-dependent experimental results obtained in both systems are shown in Sec. III, and then discussed in Sec. IV.

II. EXPERIMENTAL APPARATUS AND PROCEDURES

The experimental setup for system A was the same as that used in the bibliography [26–28] and can be seen sketched in Fig. 2. We refer to these articles for further details. For system B, an ''inhomogeneous heating'' [30] vessel was con-
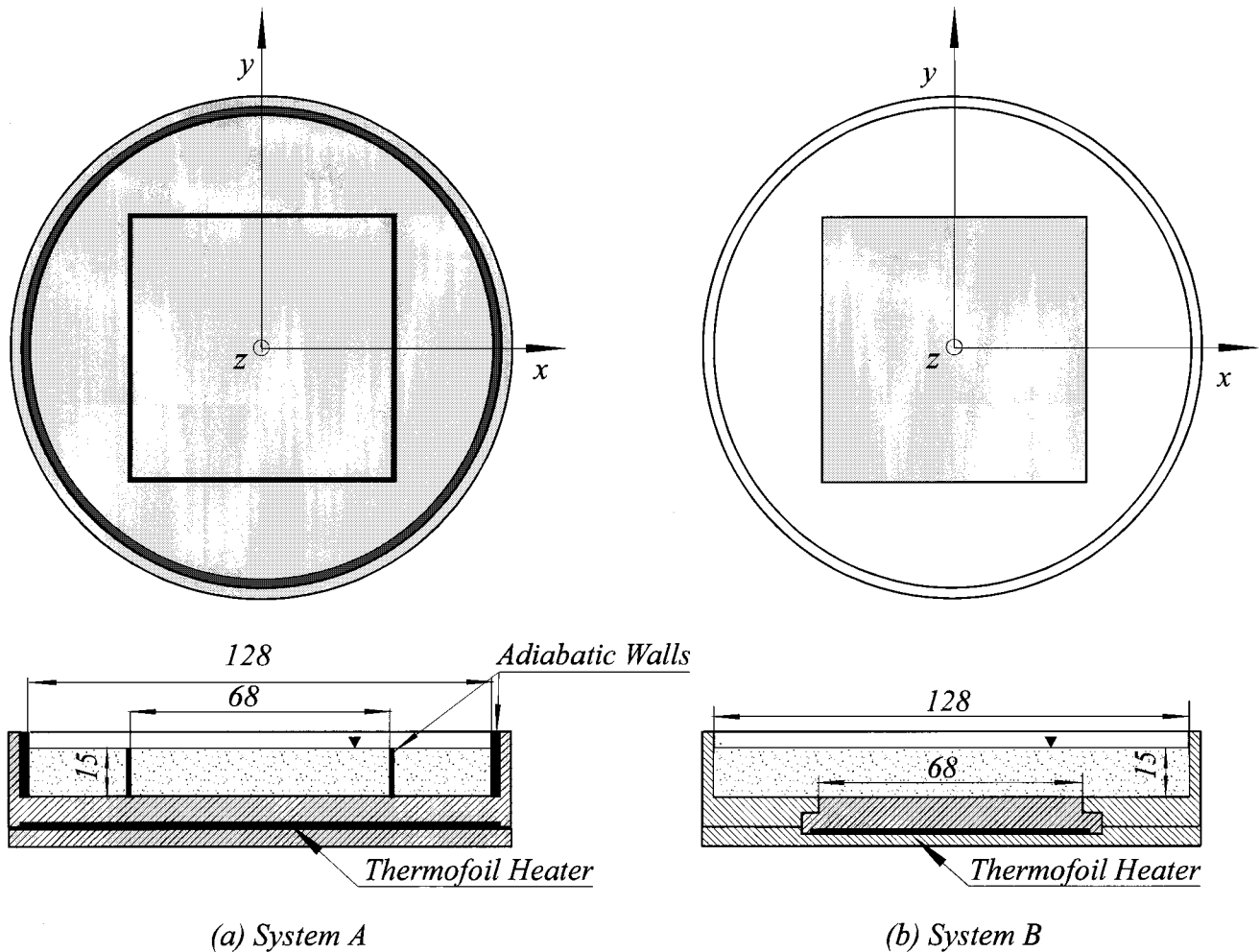

FIG. 2. (a) Plan view and cross section of system A vessel. (b) Plan view and cross section of the system B vessel.

structed. A thin film Thermofoil heater was inserted in a square aluminum bore (68×68 mm) at 10 mm under the surface contacting the fluid. The bore with the heater is tightly mounted in a square hole of a plastic container as is shown in Fig. 2(b). A plane surface of 128 mm diameter is defined by the aluminum heater and the bottom part of the plastic (Delrin polycarbonate) container with cylindrical lateral walls. A very accurate level of heating power can be fixed with a regulated power supply that then keeps the power constant. The obtained temperature profile is uniform (±0.01 K) over all of the heater plate.

Silicon oil with 350 cSt (Pr=3080) was used in both experiments (the same as in Ref. [26]). Several properties have been measured in our laboratory, including the refraction index thermal coefficient ($\partial n/\partial T$), and can be considered approximately constant over all the temperatures studied here.

In the experiments, depth was measured introducing a micrometer inside the fluid. The surface position was detected by the shadowgraph system and the heater surface was detected by electrical contact with the aluminum plate. Error in depth is therefore less than 5 μm. Temperature profiles with depth were obtained by a computer controlled precision positioner moving a thermocouple sensor in vertical steps.

The parallel beam shadowgraph device used to see the plan form was described in Ref. [23]. A digital image processing system coupled to this setup was used. Software was developed to measure a distance between two points on a prefixed line of pixels as XX or YY, in Fig. 5(c). Intensity of the pixel line was stored each second, and a spatiotemporal diagram can be constructed, as appears in the figure.

At fixed positions, temperature data files were obtained with small thermocouples and infrared sensors. Data acquisition systems (HP 1347A and Fluke 2620 "Hydra") were used to record the temperature data files. In all the results presented here, the typical Fourier spectra in time-dependent convection states are obtained from signals with more than 200 periods after the stabilizing time (this means several hours of measurements for each one).

When plan-form and temperature measurements had been performed simultaneously, care was taken to avoid a perturbation of the flow by the thermocouples. To identify and minimize this interaction, patterns were simultaneously monitored when temperature measurements were being performed. When interaction was unavoidable (as in near surface measurements), a noninvasive infrared sensor was used. The target area of this sensor is at least twice the interaction area of thermocouples, so infrared measurements reflect a medium value over a larger region (typical thermocouple size is 0.5 mm).

Surface profiles were measured by reflecting on the fluid surface a straight line obtained from a He-Ne laser with a cylindrical lens beam expander, as sketched in Fig. 3(a). Reflection at a long distance is spatially filtered and recorded with a charge-coupled device (CCD) camera. Our image acquisition software can measure the $z_0(t)$ value [Fig. 3(b)] where z_0 indicates the maximum amplitude in surface deformation. The straight line defined by the laser beam can be placed in any place on the container surface. Results presented here correspond to an XX diameter in system B [Fig. 5(c)]. Maximum deformation amplitude was calibrated with the same micrometer device used in depth measurements.
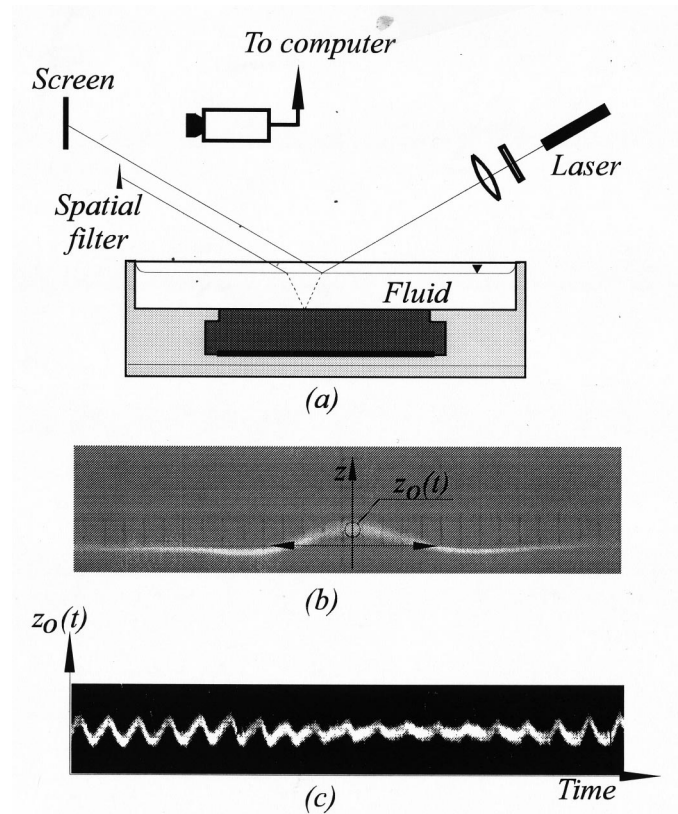

FIG. 3. (a) Experimental setup used to measure dynamical surface deformation used in both systems. (b) Typical surface profile obtained at a long distance in system B. (c) Time-dependent signal obtained in system B by measuring the maximum deformation with the data acquisition system (Ra/Ra$_0\approx$80).

When the curvature becomes time dependent, a signal proportional to this curvature amplitude can be obtained at the center of the pattern as shown in Fig. 3(c).

When the laser sheet is vertical and the fluid is sparsely seeded with small size particles, the streamlines of the flow can be observed integrating the scattering of the laser beam with a second CCD camera. Considering that particles follow the flow without delay [31], image particle velocimetry can be used to obtain the mean velocity profile on the illumination plane. The results will be shown in the next section.

A. Steady state patterns: Flows, temperatures, and surface deformation

Different patterns appear in small aspect ratio containers with homogeneous heating when the aspect ratio is modified [22,23]. With square boundary conditions, four symmetrical cells are obtained near threshold when the aspect ratio is approximately 4.5. We used this aspect ratio in both systems. Considering threshold values obtained from the Nield theory in the equation: Ma/Ma$_0$+Ra/Ra$_0\cong$1, the proportion between surface tension and buoyancy for the fluid used is 20%+80%, respectively. As depth was kept constant, this ratio is the same for all the experiments and the system is always on a straight line in the space Ma/Ma$_0$ vs Ra/Ra$_0$ when temperature gradient is the control parameter (the "physical line" described in Ref. [8]).

Very few experimental observations are reported in systems where the bottom surface is partially heated (''inhomogeneous heating'' [30,32]). Interest arises mostly from applications in laser heating and crystal growing. A quantitative comparison of our experiments with earlier studies is not possible, because a different visualization method (aluminum powder seeding) was used by these authors. Nevertheless, we obtained the same number of cells, plan form, and thermal waves for similar Rayleigh numbers. The existence of instability regions with hydrothermal waves was reported in Ref. [30].

In the experiments considered here, patterns corresponding to steady state situations remain stable if the heater temperature is fixed. The stationary condition was checked by running experiments for more than 8 h each time and each pattern several times.

1. System A

In system A, when the convective steady state is reached, a stationary pattern composed of four cells appears. The plan form visualized by shadowgraph is shown in Fig. 4(a). We here consider ''a cell'' to be a fluid region limited by liquid cold walls (liquid flowing down). In the shadowgraph diagrams, cold lines appear as sharp white lines. Fluid is not strongly mixed between cells. To check that this was so, we carried out seeding with aluminum powder in one cell and observed that the aluminum remained trapped there for several days.

In this system, a small change in the focal distance of the shadowgraph apparatus does not essentially change the shape of the plan form, because a true cold wall descending from the free surface to the bottom of the container exists. The behavior of this system when the control parameter (temperature gradient) is increased was given in Ref. [28]. Distance d measured on the plan form [Fig. 4(a)] was used as a representative variable of the developments in time. This system has four principal regions where flow goes up, all located on the diagonals of the square. If a small quantity of a dye is injected inside the fluid a complicated streamline can be seen [Fig. 4(b)]. A streak photograph of the flow on the surface obtained by seeding with aluminum powder is shown in Fig. 4(c), partially superimposed by a sketch of velocity vectors obtained by numerical simulation [33]. Surface deformation in this system is negligible compared with system B.

2. System B

In steady state convection, a pattern like that in Fig. 5 can be observed. Changing the focus in the shadowgraph system, the pattern changes from Fig. 5(a) focused on the free surface, to the pattern focused near the heater plate shown in Fig. 5(b). We used the first as representative, because oscillation is greater and can be observed better. Distance a in the core of Fig. 5(c) was used in this system as the variable that becomes modulated in amplitude when the time-dependent regime is reached. Space-time diagrams reported in Fig. 5(c) show the stationary condition of a in the selected XX line.

Flow on a horizontal plane (x,y) is sketched in Fig. 6(a) near the free surface and in Fig. 6(b) near the bottom of the cell. A streak photograph of the streamlines in the XX vertical cross section can be observed in Fig. 6(c). This figure
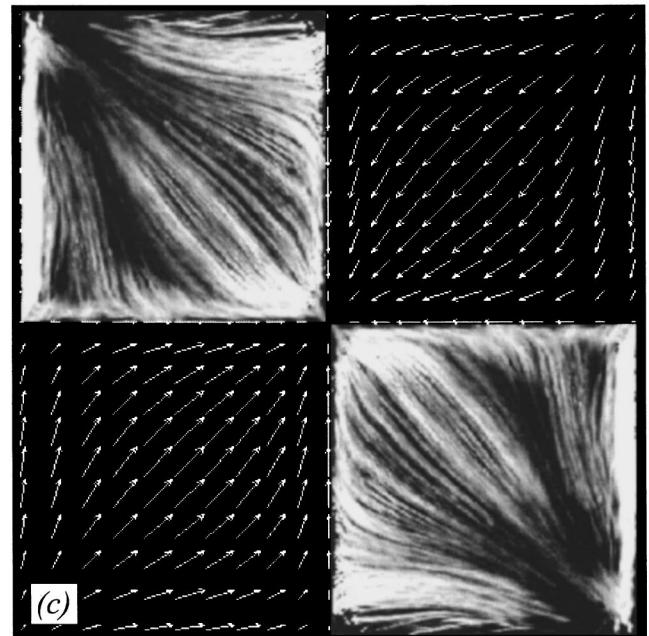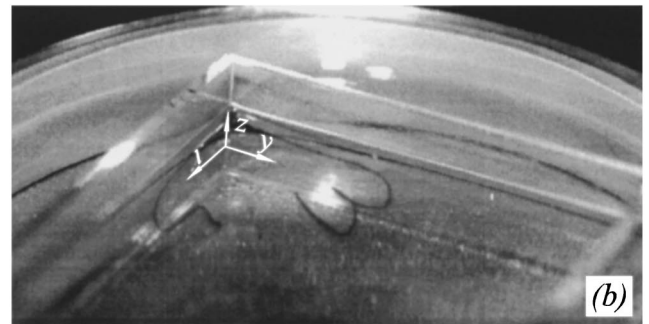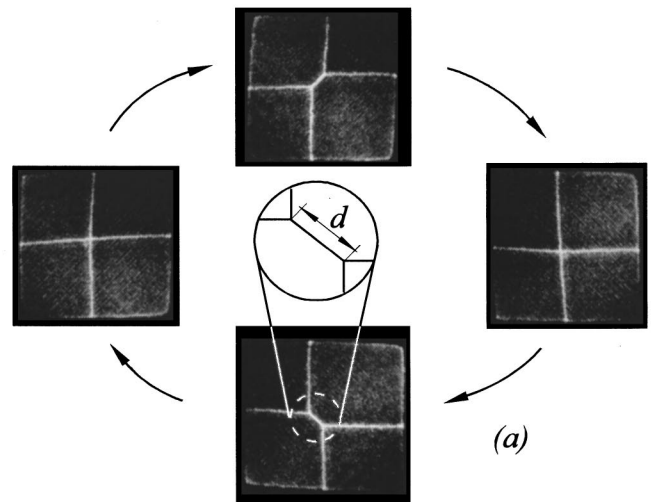

FIG. 4. System A: (a) Plan-form photographs. There is no great difference in the plan form between bottom and surface focusing. (b) Photography of a streamline in system A obtained with a dye drop injected near the surface at the corner ($Ra/Ra_0 \approx 20$). (c) Flow on the surface obtained by seeding with aluminum powder superimposed with a sketch of velocity vectors obtained by numerical simulation [39] on the other diagonal ($Ra/Ra_0 \approx 20$).
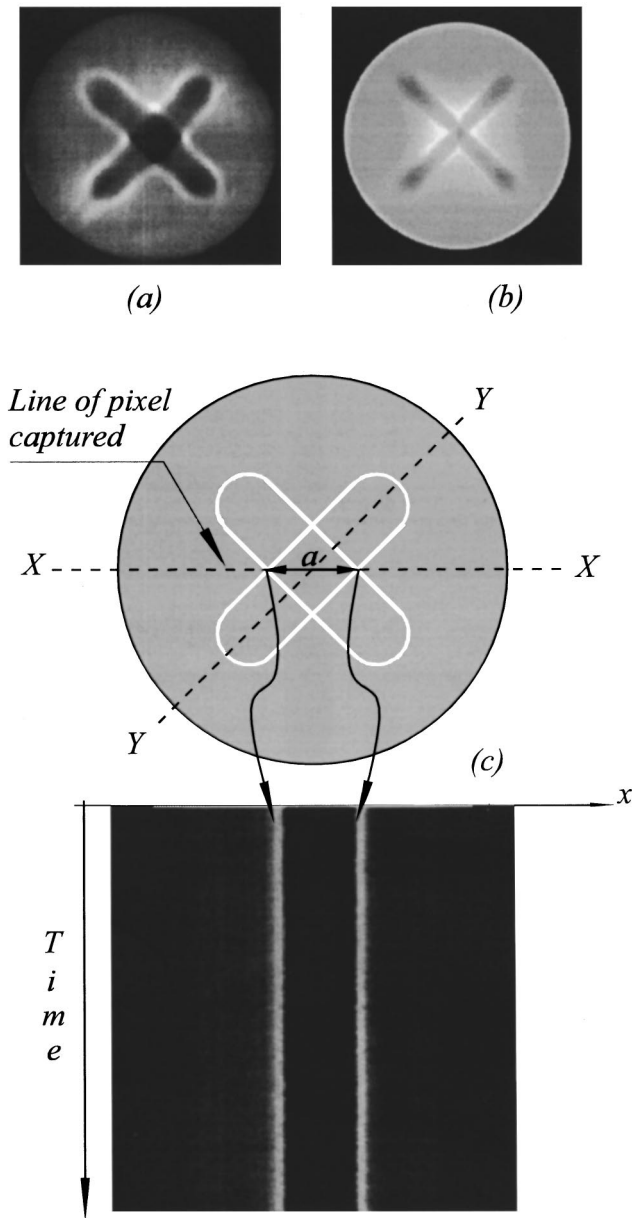
(a)   *(b)*

(c)

FIG. 5. (a) Plan form of system B obtained by focusing on the free surface. (b) Plan form obtained by focusing near the heater plate. (c) Space-temporal diagram obtained from a line of pixels XX in (a). Space variable a remains constant below the time-dependent threshold (Ra/Ra$_0 \approx$45).

shows the left part of the vessel near the center of the heater. The particles in the flow come from the left near the bottom, and then return to the left near the surface. Flow goes upward also on diagonals of the square heater. The photograph observed in Fig. 6(d) was obtained by three exposures with the same sampling period (YY cross section). The difference in the distance between the three brightness regions shows that horizontal velocity on the diagonals decreases toward the center. Particle velocity profiles $V_x(z)$ at $x=17$ mm from the center of symmetry on the XX plane and a temperature profile $T(z)$ for the same point are shown in Fig. 7. Temperature of the heater (T_c) was fixed near the time-dependent convection threshold.

If attention is fixed on where the warm flow goes up instead of where the cold flow goes down (as in system A), we

(a) Streamlines near the surface   **(b) Streamlines near the bottom**

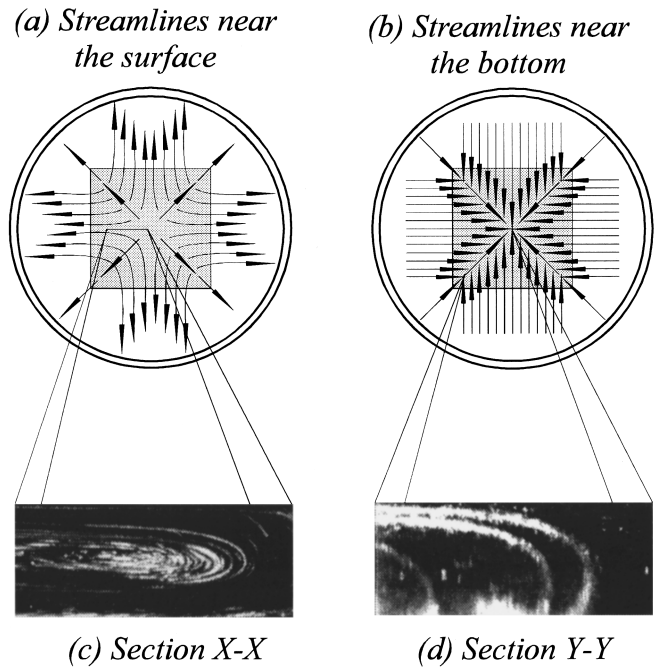

(c) Section X-X   **(d) Section Y-Y**

FIG. 6. (a) Scheme of streamlines near the surface in system B. (b) Scheme of streamlines near the bottom. (c) Streak photograph of the streamlines on a vertical cross section in the XX position obtained by seeding aluminum powder (Ra/Ra$_0 \approx$45). (d) Streak photograph along diagonal YY (three exposures) (Ra/Ra$_0 \approx$45).
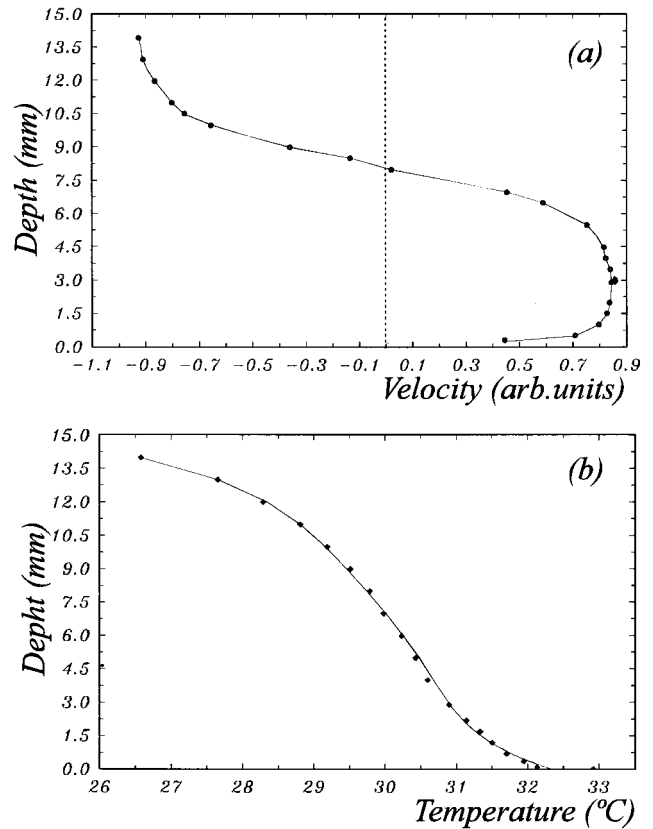

FIG. 7. System B: (a) Average horizontal velocity V_x under the time-dependent threshold as a function of altitude from the heater plate, measured on a vertical line at 17 mm from the center of symmetry (Ra/Ra$_0 \approx$20). (b) Vertical temperature profile at the same position.
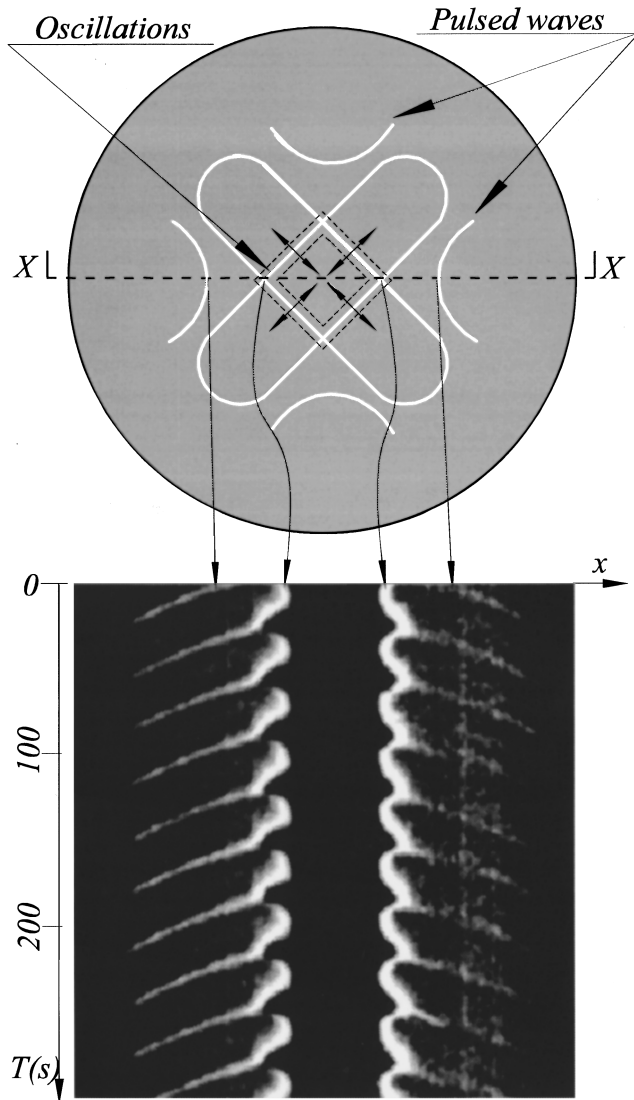
FIG. 8. System B (Ra/Ra$_0$≈70): Time-dependent regime observed on the plan form. The spatiotemporal diagram shows a plan-form oscillation where distance a becomes time dependent. A front of traveling waves appears from the threshold.

observe that in this system too, the heater is divided into four regions. Cell boundaries are now defined by flows going upward on the diagonals of the square (diameter YY of the convective container). But as can be seen from the former figures, at the center of the heater the flow of the four cells gives the strongest upward flow region of the system. Consequently, a large stationary surface deformation (~ 300 μm) near the time-dependent convection threshold [Fig. 3(b)] appears. Surface deformation produces the shape of the plan form observed when the shadowgraph apparatus is focused at the surface [Fig. 5(a)]. Curvature also becomes modulated when the oscillatory threshold is reached. No strong deformation is observed on diameter YY outside the central core.

III. TIME-DEPENDENT REGIME: EXPERIMENTAL RESULTS

A. Phenomenology

When the power applied to the heater is increased, the bottom plate temperature rises slowly and the time-
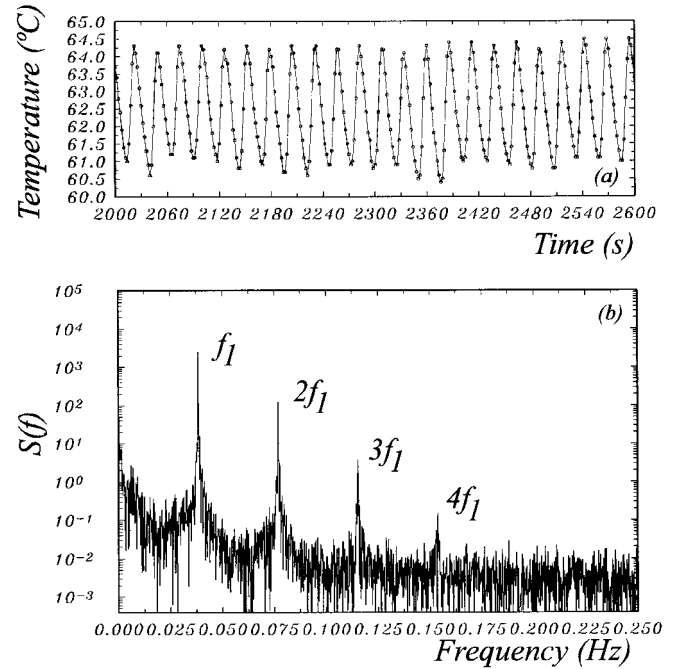

FIG. 9. System B (Ra/Ra$_0$≈60): (a) Temperature signal obtained near the bottom ($z=1$ mm) at the center of symmetry. (b) Fourier power spectrum of the temperature signal. Please note that the signal shows only one frequency (and its harmonics).

dependent convection threshold is exceeded in both systems when power density is ~ 1 W/cm^2. No hysteresis was observed at threshold. The oscillatory dynamic is the same irrespective of whether the time-dependent regime has been reached by increasing the power slowly, in small steps, or suddenly in one step.

1. System A

The time-dependent convection regime for system A was analyzed in [25–28]. We remember that threshold for this regime was ~ 60 °C measured at the heating plate, with ambient temperature near the surface $T_a=21$ °C, Ra=52,5Ra$_0$, calculated with reference to the Nield theory threshold: Ra$_0$=550, Ma$_0$=14,5. When the oscillatory regime begins, d becomes amplitude modulated. As d amplitude is the change in the total length of a cold wall during an oscillation, it is also a measure of the convective flow modulation.

2. System B

System B begins to oscillate when the bottom temperature is also near ~ 60 °C. The characteristic dimension a of the central core is now amplitude modulated from the maximum of the steady state value. A spatiotemporal diagram in Fig. 8 shows when the stationary value of a [Fig. 5(c)] begins to oscillate. During an oscillation period a increases its value and then relaxes to the original one.

The followings facts can be observed.

(a) The plan form oscillates. The central core of Fig. 5(c) changes its length a periodically as is shown in the spatiotemporal diagram in Fig. 8.

(b) If temperature is measured at the plan-form center of symmetry and near the bottom plate (1 mm), its value begins
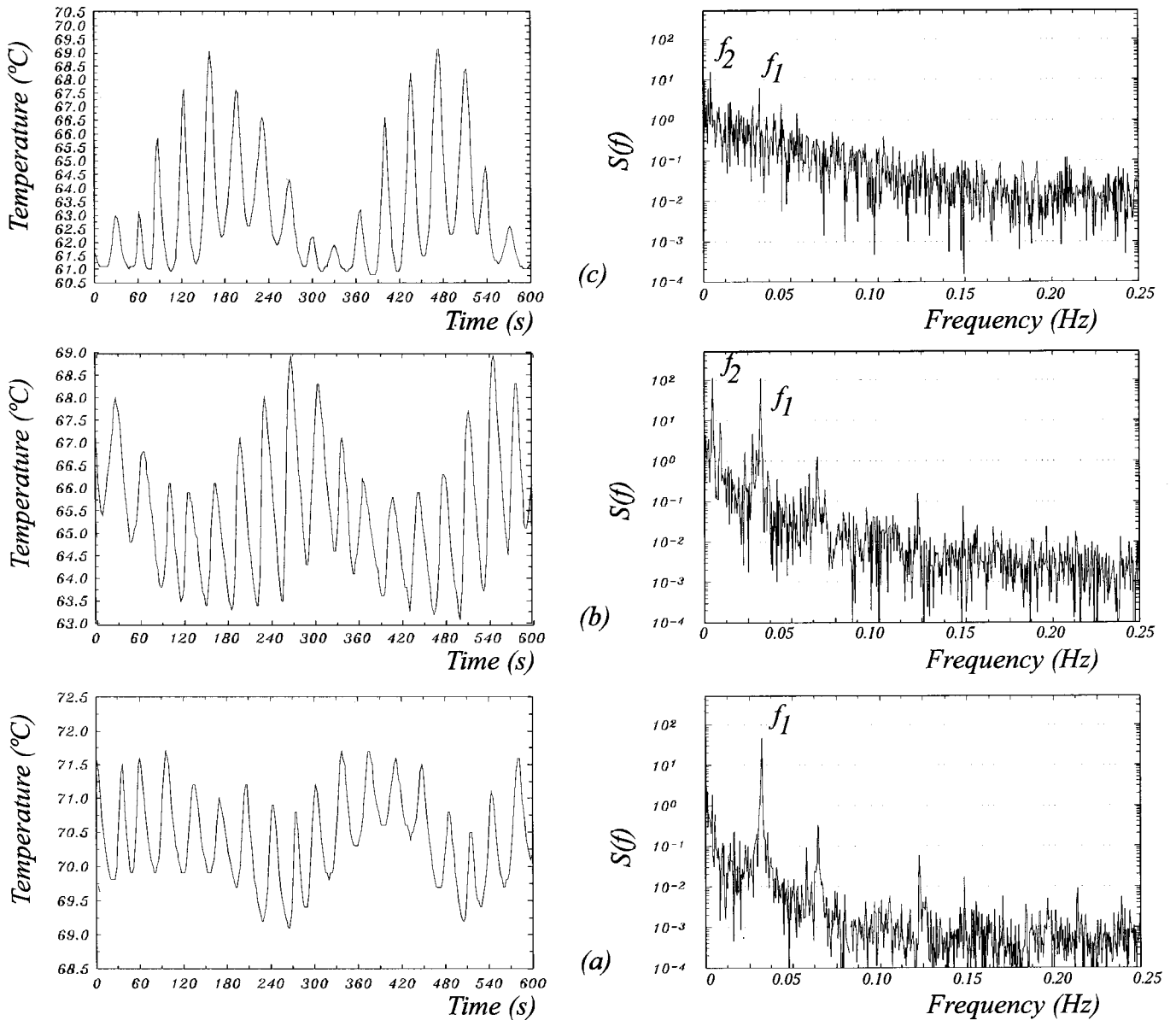
FIG. 10. System B ($Ra/Ra_0 \approx 70$): (a) Temperature signal and power spectrum near the bottom plate ($z=2.2$ mm) at the center. Frequency f_1 is dominant. (b) Temperature signal and power spectrum at an intermediate position ($z=8$ mm). Amplitude of frequency f_1 is similar to the amplitude of a new frequency f_2. (c) Temperature signal and power spectrum near the surface ($z=14$ mm). Frequency f_2 is dominant.

to oscillate together with the plan form. A typical signal near threshold is shown in Fig. 9. Within an error of 3%, planform and temperature oscillation thresholds are the same.

(c) If temperature signal dependence with depth is analyzed at the center of symmetry (that is, the strongest flow region), the results presented in Fig. 10 are observed. The density power spectrum shows two main frequencies, one predominating near the bottom [$f_1 \sim 0.03$ Hz, in Fig. 10(a)], the other near the free surface [$f_2 \sim 0.003$ Hz, in Fig. 10(c)]. At mid depth, the amplitudes of both frequencies are comparable [Fig. 10(b)]. Amplitudes in the power density spectra against depth are plotted for both frequencies in Fig. 11. The maximum for the second frequency f_2 corresponds to the position where the sign of $V_x(z)$ changes.

(d) The amplitude of the surface deformation at the center of the plan form $z_0(x)$ also begins to oscillate with the plan form and temperature. The surface oscillates, changing its maximum static amplitude $z_0(x=0)$ near the time-dependent
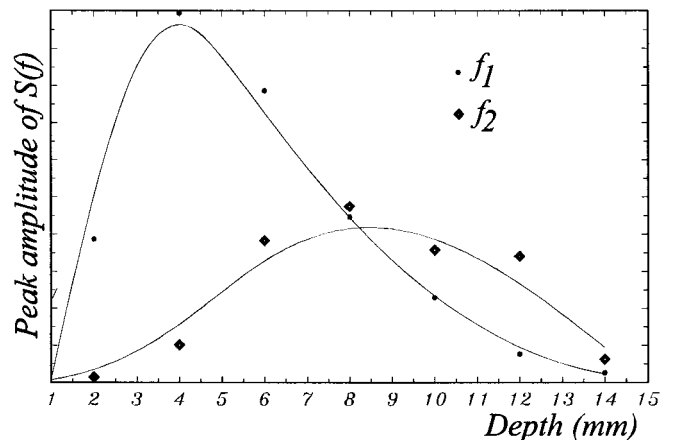

FIG. 11. System B ($Ra/Ra_0 \approx 70$): Amplitude of power spectrum main frequencies component f_1, f_2 plotted against depth ($z=0$, heater plate and $z=15$ mm free surface).
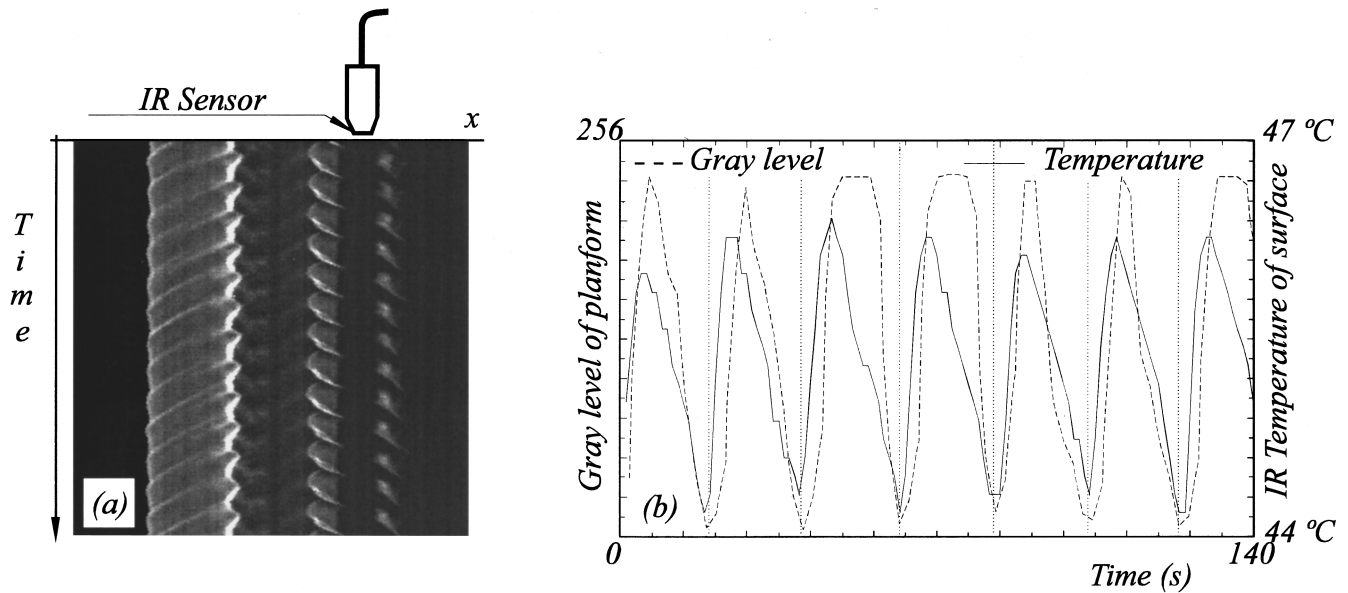
FIG. 12. System B (Ra/Ra$_0$≈70): Plan-form and temperature signals compared. (a) Position of the IR temperature sensor can be observed by a shadow in the spatiotemporal diagram. (b) Superimposition of temperature and plan-form signals in order to show that both have the same period.

threshold and also its curvature motivated by the simultaneous change in (a). With the setup described in Sec. II, a cut of the surface can be obtained by reflecting a laser beam. A time-dependent signal corresponding to the amplitude $z_0(t)$ was shown in Fig. 3(c).

(e) When a is at the maximum, a surface perturbation generated by the oscillation propagates as a traveling wave in the flow direction (Fig. 8). This perturbation acts as a pulse that can be easily observed by white lines in the spatiotemporal diagram. Velocity can be measured point by point from this diagram but some corrections in distance must be introduced to avoid errors caused by the meniscus at the lateral walls.

The first question about whether plan-form oscillations have the same period as temperature or not can be roughly answered with Fig. 12, where the temperature signal is compared with a variable obtained from plan-form oscillations. A more exact comparison is obtained by considering Fourier spectra at a fixed point of the control parameter, using longer data files (Fig. 13), where harmonic superposition also appears. Plan-form oscillations are coupled with frequency f_1 of the temperature signal, even if near the surface the predominating frequency in signals is f_2 (which seems coupled to the flow).

Coincidence exists in the whole range of control parameters studied here ($52\text{Ra}_0 < \text{Ra} < 98\text{Ra}_0$). In this range, any variable can be used to describe the temporal behavior and used to obtain information about the others. But if we increase the control parameter further toward turbulence, correlation among spatial and temperature variables must be checked. For higher Rayleigh numbers signals from spatial variables and temperature become uncorrelated.

B. Identifying oscillators

Different methods have been used in Rayleigh-Bénard convection to identify where the sources of the spectrum are located. In this study we scanned the convective horizontal cell until a maximum for the temperature signal (peak to peak) was reached.

In system A, there are four spots (one for each cell) corresponding to the maximum amplitude in temperature oscillation located on the diagonals (the warmest regions correspond to dark zones in the plan form). When the time-dependent onset is reached, the four spots begin to oscillate simultaneously. The signals obtained from them are principally coupled by pairs in opposition of phase, even when a complex temporal behavior exists [34].

System B has also four cells, but the maximum amplitude in temperature oscillations is centered here with the plan-form center, disappearing sharply outside the central region on the axis XX and gradually on the diagonal YY. Fluid here flows up on diagonals [a component of vertical velocity (V_z)
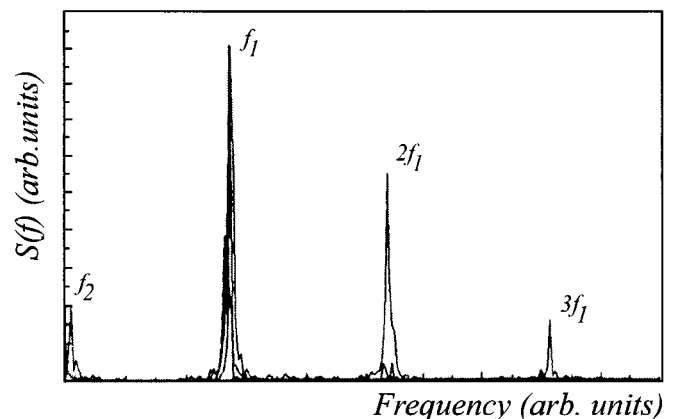

FIG. 13. Power spectrum superimposition of signals obtained from temperature, plan-form, and surface curvature in System B (Ra/Ra$_0$≈70). Peak corresponding to f_2 only appears in the temperature spectrum. Control parameter is near time-dependent threshold.
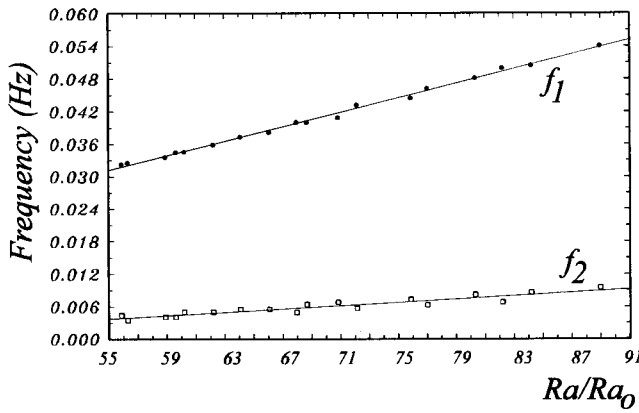
FIG. 14. Frequency dependence against Rayleigh number in system B.

exists as shown in Fig. 6] dividing the vessel above the heater surface into four cells with warm walls. The heating is reinforced in the central region by contributions of these cells, making the center of symmetry the warmest region where the oscillation amplitude is maximum. In system A, this is a cold region by influence of the lateral boundary conditions.

We also studied in system B the behavior of the two main oscillation frequencies f_1 and f_2 against the temperature of the thermal heater T_c (proportional to the Rayleigh number). The temperature signal was measured in the region near ($z=8$ mm, $x=0$, $y=0$) with z measured from the bottom plate, where the two main frequencies in the power density spectrum are comparable [Fig. 10(b)]. As can be seen in Fig. 14, the frequency of each component has a different behavior when the heater temperature is increased.

C. Average horizontal velocity against depth $V_x(z)$

This component of velocity is interesting because it can give us an idea of the boundary layer thickness. The average horizontal velocity component as a function of depth $V_x(z)$ was measured by particle image velocimetry, 17 mm from the plan-form center on the XX diameter. Results for two different temperatures beyond the time-dependent threshold are shown in Fig. 15. Amplitude and position of the maxi-
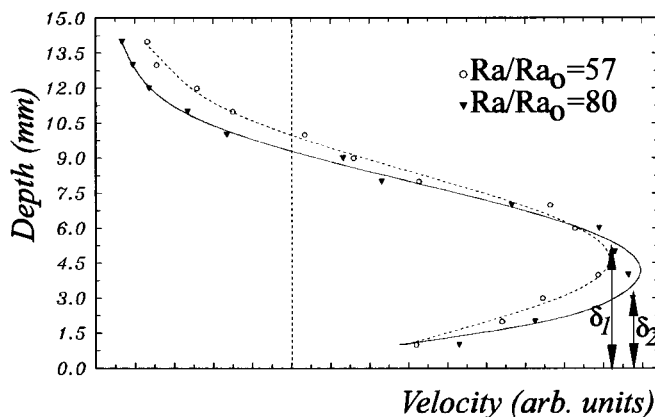

FIG. 15. Average horizontal velocity profiles obtained for two Rayleigh numbers in system B. A lower value for the boundary layer thickness δ_2 is obtained for higher Rayleigh numbers.

mum in the profile are functions of the heater temperature. The maximum goes down to positions near the heater plate when temperature increases. The instantaneous velocity $v(t)$ at each position oscillates around the mean values of Fig. 15. We observed this behavior, but our image processing system is not yet able to obtain quantitative results. The main feature to recall here is the descent of position δ corresponding to the V_x maximum, because this indicates a fall in the boundary layer thickness with temperature. In spite of the fact that we cannot yet give a quantitative measurement of the boundary layer thickness obtained directly from velocity measurements, this qualitative behavior reinforces arguments about the origin of the oscillation as will be discussed in the next section.

IV. DISCUSSION

Both systems were constructed with the same geometry and the same kind of fluid was used. Different lateral boundary conditions, one closed and the other open to lateral exchanges, give rise to different flows and patterns. Despite these facts, the time-dependent regime has the same threshold (considering an error of less than 3%) and a similar oscillation frequency in the plan form and in temperature. This coincidence can be explained if a common mechanism of instability is responsible for temporal dependence.

If the fluid layer in both systems is considered from the point of view of heat transport, the heater supplies energy at a constant rate at the bottom and the heat flow at the output is amplitude modulated (approximately 10%). As we have mentioned, periodic energy storage is accomplished in the fluid layer and this energy storage mechanism will be responsible for temporal behavior modulating the flow in amplitude. In fluids with a high Prandtl number, there are very few transient energy storage mechanisms in the convective layer, that is, boundary layer modulations, thermal plumes, and thermals [29].

We suggested that a boundary layer instability could be the origin of the time-dependent regime as in high Prandtl number Rayleigh-Bénard convection. Considering the Howard theory where the boundary layer modulation is attributed to a Rayleigh-Bénard mechanism, a simple diffusion expression relates the boundary layer thickness δ with the typical period of the oscillations T and the thermal diffusivity of the fluid κ: $\delta = \sqrt{\pi \kappa T}$ [18]. With this expression, the thickness of the boundary layer can be obtained if a typical period in a given fluid is known (as in Ref. [16]). Considering the fluid used here and the periods obtained from temperature signals or plan-form oscillation measurements, the boundary layer thickness must be ~ 2.5 mm, if Howard's instability controls the time-dependent regime.

As a theory obtained from hydrodynamic equations to check this value is still lacking, we looked for experimental confirmation. Different techniques could be used to accomplish this, but experimental restrictions rule out several of them. For example, a nonperturbative direct measurement like lateral interferometry used in Ref. [16] is not possible here, because a long optical path through different flow regions exists from the lateral walls to the oscillating region. A laser beam crossing the cell is also strongly curved to the bottom (lower density regions) and cannot be used. As direct

temperature measurement performed with sensors inside the boundary layer can introduce strong perturbations, we decided to evaluate this thickness by using the velocity profile measurements. Taking as the boundary layer limit (as usual) the altitude z corresponding to the maximum in the experimental velocity profiles $V_x(z)$ obtained in Sec. III, this value is approximately the same as previously obtained by the Howard expression, when a typical period from temperature measurements is used. Inversely, if we introduce the thickness value obtained from velocity measurements in the Howard expression, a typical temperature period $T(\delta)$ can be calculated and compared with the experiments. In spite of this coincidence that focuses the attention on the boundary layer, a detailed description of the oscillation mechanism makes necessary a more in-depth study on the instability inside the boundary layer. Until now, it has remained unclear and several new questions have arisen.

First, the boundary layer thickness obtained in these measurements corresponds to the *velocity* and the Howard mechanism was calculated with the thickness corresponding to the *thermal* boundary layer. Simple calculations give a ~1/10 ratio between them for the fluid used here [35]. Second, the Howard mechanism can explain only one (f_1) of the two main frequencies of the Fig. 10 spectrum. In Rayleigh-Bénard convection, i.e., [15,16] a similar kind of spectrum (with two main frequencies) appears. In Ref. [16] authors identify the second frequency with a thermal plume oscillator arising from the cold boundary layer (a new oscillatory mechanism) and this fact can be seen from the interferograms presented by them.

We have, instead of a cold boundary layer, a free surface in contact with air. Temperature measurements [Fig. 7(a)] do not show any cold boundary layer (on the fluid side). We must think in our case that dynamics of frequency f_2 arise from the bottom (warm) layer interacting with the flow. The flow transports the plume or "thermals" [29] generated by a periodic fluctuation in the boundary layer thickness. The higher frequency can be related to the Howard mechanism or to any other periodical (or quasiperiodical) mechanism inside the boundary layer, but the second frequency of the spectrum should also be related to the velocity of the basic flow.

Calculating the average time to a round-trip with the flow (roughly, two transit times in the XX plane), the inverse of this time approximately gives the second frequency, that is, a perturbation traveling with the flow velocity measured at a fixed point gives a similar frequency. This hypothesis is also compatible with a lower amplitude of the second frequency f_2 near the bottom plate and higher in a zone where the flow influence is greater, as was shown in Fig. 10.

Summarizing, the flow influence can be regarded as a coupling mechanism among two frequencies generated in the boundary layer or as a support for a feedback perturbation introduced in a region with amplification. Both mechanisms could give the same effect and we do not yet have a definitive result. But focusing the shadowgraph system to the bottom region, a growing front propagating with the flow to the central region can be seen. This is evidence that the oscillations arise from the boundary layer. Further detailed studies are necessary to elucidate this subject in depth.

In system A, the temporal dynamic was modeled on previous studies with a spatial variable coupled to the tempera-ture evolution. Dynamic predictions were made and, if planform shape and temperature signals remain coupled (correlated), qualitative behavior is the same for both signals. No equivalent work has been done yet for system B. Using the heat flow supplied from the bottom plate instead of the vertical temperature gradient, as was suggested in [36], and relating it to an equation for the spatial variable a, a mathematical model as in system A can be constructed. But as coupling between variables exists here in a more restricted region of the control parameter, and frequencies f_1 and f_2 have different behaviors against the Rayleigh number, this approach is less interesting. Normal mode description was performed in system A [34,33]. In system B, this approach seems harder. We do not observe a significant nonlinear combination of the two main frequencies in the Fourier spectrum near the time-dependent threshold. This means that a linear theory must give acceptable results for threshold calculations. When the control parameter is increased, the transition to turbulence in this system corresponds to a quasi-periodicity scenario, and it is still being studied.

Another new feature, traveling waves, can be observed in system B in spatiotemporal diagrams, appearing from the beginning of the time-dependent regime. Instead of a "true" wave, these "waves" may be a different density fluid drop traveling on the main flow near the free surface like a pulse. Traveling time with the flow velocity is shorter than necessary for thermal diffusion and this avoids dispersion of the pulse. Further studies are necessary to clarify this subject. In system A, waves appear only for higher Rayleigh numbers when the system is clearly in transition to turbulence. Other articles [37,38] show that these waves are related to the presence of a horizontal temperature gradient. In early studies, Krishnamurti [10] showed that for high Prandtl number fluids in Rayleigh-Bénard convection, turbulent states appear after a tridimensional convection state (where a horizontal component of gradient exists). As we saw that waves also appear in system A but for higher Rayleigh numbers [39], we suppose as a conjecture, that in this system too the horizontal gradient component becomes important in this high temperature region. In system B this component has existed since the beginning because of the geometry so these waves appear at the threshold of time-dependent convective movements. This will be further discussed elsewhere.

V. CONCLUSIONS

We show experimentally that in a Bénard-Marangoni experiment with low aspect ratio and high Prandtl number a discrete narrow-band frequency spectrum appears in the temperature signals if the bottom temperature is increased sufficiently. Other variables measured, like surface deformation or characteristic distances measured on the plan form, exhibit similar behavior and Fourier spectrum in the control parameter range here studied.

It was also shown that the oscillation regime begins in a boundary layer instability. The instability mechanism, demonstrated previously in Rayleigh-Bénard convection and Hele-Shaw cells, is confirmed here in Bénard-Marangoni convection. So it becomes a quite general mechanism present in high Prandtl number time-dependent convective systems with completely different geometries, plan forms, and lateral boundary conditions.

A clear distinction was shown between effects coming from lateral boundary conditions and those arising from thermal coupling, in spite of the fact that a detailed investigation of the instability mechanism inside the boundary layer is still lacking. Lateral boundary symmetry and characteristics (or geometry of the heater in the unhomogeneous case) are principally responsible for the internal structure of the convective cell (flow geometry) and determine the geometrical patterns observed in the plan form. Thresholds and periods in the time-dependent regime come principally from the heat coupling through the boundary layer (thickness of the layer and thermal properties) and they are not strongly influenced by lateral boundaries or by the surface curvature. In the inhomogeneous heating case, the amplitude of the main frequencies with the control parameter was determined and the oscillators located. We also reported the existence of thermal waves (or lower density spots traveling as waves), from the beginning of the time-dependent convective regime for system B, and in a higher Rayleigh number region in system A. Finally, as the different variables used (physical and geometrical) remain coupled or correlated in the control parameter region studied, a dynamic model constructed with one of them (as in Ref. [27]) is essentially valid for the others.

ACKNOWLEDGMENTS

[1] H. Bénard, Rev. Gen. Sci. (**I**), 1261 (1900); (**II**), 1309 (1900).

[2] P. Manneville, *Dissipative Structures and Weak Turbulence* (Academic, New York, 1990).

[3] M. C. Cross and P. C. Hohenberg, Rev. Mod. Phys. **65**, 815 (1993).

[4] J. E. Wesfreid and W. Zalesky, in *Cellular Structures in Instabilities*, edited by J. E. Wesfreid and W. Zalesky, Lecture Notes in Physics Vol. 210 (Springer-Verlag, Berlin, 1984).

[5] E. L. Koschmieder, *Bénard Cells and Taylor Vortices* (Cambridge University Press, Cambridge, England, 1993).

[6] D. A. Nield, J. Fluid Mech. **19**, 341 (1964).

[7] The linear theory values (Nield) have been checked experimentally in J. Pantaloni, R. Bailleux, J. Salan, and M. G. Velarde, J. Non-Equilib. Thermodyn. **4**, 201 (1979).

[8] Nonlinear theory can be found in M. Bestehorn, Phys. Rev. E **48**, 3622 (1993).

[9] M. Schatz, S. VanHook, W. McCormick, J. Swift, and H. Swinney, Phys. Rev. Lett. **75**, 1938 (1995).

[10] R. Krishnamurti, J. Fluid Mech. Part 1 **42**, 295 (1970).

[11] R. Krishnamurti, J. Fluid Mech. Part 2 **42**, 309 (1970).

[12] R. Krishnamurti, J. Fluid Mech. **60**, 285 (1973).

[13] G. Ahlers and R. P. Behringer, Prog. Theor. Phys. Suppl. No. **64**, 186 (1978).

[14] J. Maurer and A. Libchaber, J. Phys. (Paris) Lett. **40**, L-419 (1979).

[15] J. P. Gollub and S. V. Benson, J. Fluid Mech. **100**, 449 (1980).

[16] M. Dubois and P. Bergé, J. Phys. (Paris) **42**, 167 (1981).

[17] M. Dubois, M. A. Rubio, and P. Bergé, Phys. Rev. Lett. **51**, 1446 (1983).

[18] L. N. Howard, in *Proceedings of the 11th International Congress on Applied Mechanics*, edited by H. Gortler (Springer-Verlag, Berlin, 1966), p. 1109.

[19] J. W. Elder, J. Fluid Mech. **32**, 69 (1968).

[20] A. A. Townsend, J. Fluid Mech. **5**, 209 (1959); G. E. Willis and J. W. Deardorff, Phys. Fluids **10**, 931 (1967).

[21] M. A. Rubio, P. Bigazzi, L. Albavetti, and S. Ciliberto, J. Fluid Mech. **209**, 309 (1989).

[22] E. L. Koschmieder and S. Prahl, J. Fluid Mech. **215**, 571 (1990).

[23] T. Ondarçuhu, J. Millán-Rodriguez, H. L. Mancini, A. Garcimartin, and C. Pérez-García, Phys. Rev. E **48**, 1051 (1993).

[24] J. D. Crawford and E. Knobloch, Annu. Rev. Fluid Mech. **23**, 341 (1991).

[25] H. L. Mancini, Doctoral Thesis, Universidad de Navarra, Spain, 1994.

[26] T. Ondarçuhu, G. Mindlin, H., Mancini, and C. Pérez-García, Phys. Rev. Lett. **70**, 3892 (1993).

[27] T. Ondarçuhu, G. Mindlin, H. L. Mancini, and C. Pérez-García, J. Phys. Condens. Matter **6**, 427 (1994).

[28] G. Mindlin, T. Ondarçuhu, H. L. Mancini, C. Pérez-García, and A. Garcimartin, Int. J. Bifurc. Chaos **4**, 1121 (1994).

[29] J. S. Turner, *Buoyancy Effects in Fluids* (Cambridge University Press, Cambridge, England, 1979).

[30] A. Ezersky, A. Preobrazhensky, and M. Rabinovich, Eur. J. Mech. B Fluids **10**, 211 (1991).

[31] L. Hesselink, Annu. Rev. Fluid Mech. **20**, 421 (1988); R. Adrian, *ibid.* **2**, 261 (1991).

[32] A. Gaponov-Grekhov and M. Rabinovich, *Nonlinearities in Action* (Springer-Verlag, Berlin, 1992).

[33] D. Maza, B. Echebarria, C. Pérez-García, and H. L. Mancini, Phys. Scr. **T67**, 82 (1996).

[34] M. Huerta, D. Krmpotic, G. Mindlin, D. Maza, H. L. Mancini, and C. Pérez-García, Physica D **96**, 200 (1996).

[35] E. Guyon, J. P. Hulin, and L. Petit, *Hydrodinamique Physique* (CNRS, Paris, 1991).

[36] C. Normand, Y. Pomeau, and M. G. Velarde, Rev. Mod. Phys. **49**, 581 (1977).

[37] A. Ezersky, A. Garcimartin, J. Burguete, H. L. Mancini, and C. Pérez-García, Phys. Rev. E **47**, 1126 (1993).

[38] A. Ezersky, A. Garcimartin, H. L. Mancini, and C. Pérez-García, Phys. Rev. E **48**, 4414 (1993).

[39] H. Mancini (unpublished).